

Modelling the Gamma-Ray Morphology of HESS J1804–216 from Two Supernova Remnants in a Hadronic Scenario

K. Feijen¹*, S. Einecke¹, G. Rowell¹, C. Braiding²†, M. G. Burton^{2,3}, G. F. Wong^{4,2}

¹*School of Physical Sciences, University of Adelaide, Adelaide, SA 5005, Australia*

²*School of Physics, The University of New South Wales, Sydney, NSW 2052, Australia*

³*Armagh Observatory and Planetarium, College Hill, Armagh BT61 9DG, UK*

⁴*Western Sydney University, Locked Bag 1797, Penrith South DC, NSW 2751, Australia*

Accepted XXX. Received YYY; in original form ZZZ

ABSTRACT

HESS J1804–216 is one of the brightest yet most mysterious TeV γ -ray sources discovered to date. Previous arc-minute scale studies of the interstellar medium (ISM) surrounding this TeV γ -ray source revealed HESS J1804–216 is likely powered by a mature supernova remnant (SNR) or pulsar, hence its origin remains uncertain. In this paper, we focus on the diffusive escape of cosmic-ray protons from potential SNR accelerators. These cosmic rays interact with the ISM to produce TeV γ -rays. We utilise the isotropic diffusion equation solution for particles escaping from a shell, to model the energy-dependent escape and propagation of protons into the ISM. This work is the first attempt at modelling the spatial morphology of γ -rays towards HESS J1804–216, using arc-minute ISM observations from both Mopra and the Southern Galactic Plane Survey. The spectral and spatial distributions of γ -rays for the two nearby potential SNR counterparts, SNR G8.7–0.1 and the progenitor SNR of PSR J1803–2137, are presented here. We vary the diffusion parameters and particle spectrum and use a grid search approach to find the best combination of model parameters. We conclude that moderately slow diffusion is required for both candidates. The most promising candidate to be powering the TeV γ -rays from HESS J1804–216 in a hadronic scenario is the progenitor SNR of PSR J1803–2137.

Key words: ISM: cosmic-rays – gamma-rays: ISM – ISM: individual objects (HESS J1804–216)

1 INTRODUCTION

The High Energy Stereoscopic System (H.E.S.S.) has a sensitivity to γ -rays of energy 100 GeV to tens of TeV. H.E.S.S. has identified numerous γ -ray sources in the Milky Way (or ‘galactic sources’), however, the exact nature of over 30% of these sources remains unknown (H. E. S. S. Collaboration et al. 2018a). These sources are also possibly the sites of cosmic-ray (CR) accelerators, the population of these sources are dominated by objects within their final stages of stellar evolution.

HESS J1804–216 is one of the brightest unidentified TeV γ -ray sources detected, with a soft spectral index of $\Gamma=2.69$. The GeV γ -ray source, 3FHL J1804.7–2144e, was detected at the same location as the TeV γ -ray source HESS J1804–216 (see Fig. 1).

In a previous paper (Feijen et al. 2020), we studied the interstellar medium (ISM) towards HESS J1804–216 in detail at arc-min scales, to help determine the nature of the γ -ray emission. We investigated multiple plausible CR accelerators and concluded that a mature supernova remnant (SNR G8.7–0.1 or the progenitor SNR of PSR J1803–2137) or a pulsar (PSR J1803–2137) are viable accelerators of CRs to produce the TeV γ -ray emission in the hadronic and leptonic scenarios, respectively. The hadronic production of γ -rays

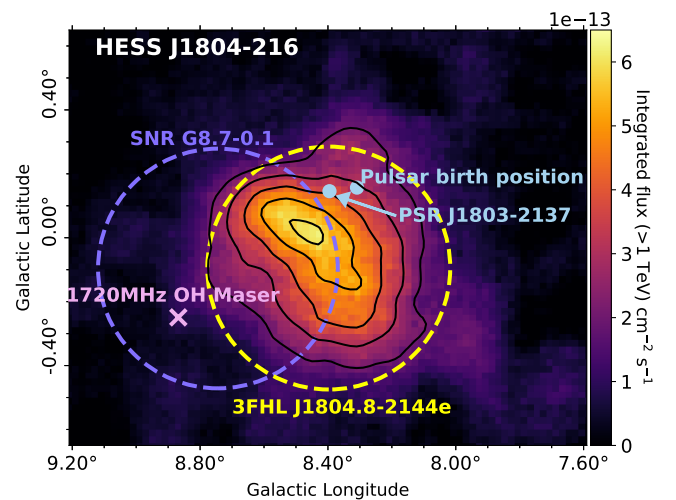


Figure 1. Integrated flux map ($\text{cm}^{-2} \text{s}^{-1}$) above 1 TeV adapted from H. E. S. S. Collaboration et al. (2018a). The dashed purple circle indicates SNR G8.7–0.1, the purple cross indicates the 1720 MHz OH maser and the progenitor SNR of PSR J1803–2137 is indicated by the blue dot. The TeV γ -ray emission from H. E. S. S. Collaboration et al. (2018a) is shown by the solid black contours (2×10^{-13} to $6 \times 10^{-13} \text{ cm}^{-2} \text{ s}^{-1}$ levels).

* Email: kirsty.feijen@adelaide.edu.au

† Presently at: Australian Space Agency, Adelaide, Australia

involves accelerated CR protons interacting with the ISM to produce γ -rays through neutral pion decay (Ackermann et al. 2013). The leptonic scenario primarily involves TeV emission being produced by inverse-Compton upscattering by highly energetic electrons. The TeV emission from HESS J1804–216 could be produced by high-energy electrons from a pulsar wind nebulae (PWNe) powered by PSR J1803–2137 (H. E. S. S. Collaboration et al. 2018b), as supported by the high spin-down luminosity. The modelled energy spectra of CR protons towards both SNR G8.7–0.1 and the progenitor SNR of PSR J1803–2137 matched with GeV and TeV observations, making it plausible for either SNR to generate the GeV and TeV γ -ray emission from HESS J1804–216.

SNRs are a typical candidate in accelerating CR protons at their shock front (Blandford & Ostriker 1980). The hadronic production of γ -rays is investigated in this paper, assuming either SNR G8.7–0.1 or the progenitor SNR of PSR J1803–2137 (shown in Fig. 1) are the plausible CR accelerators. A 1720 MHz OH maser is present at the southern edge of SNR G8.7–0.1 at 36 km s^{-1} indicating the SNR (at a velocity of 35 km s^{-1}) is interacting with the ISM (Hewitt & Yusef-Zadeh 2009).

Models of the γ -ray emission from escaping CRs have previously been presented for different γ -ray sources, such as Casanova et al. (2010) for SNR RX J1713.7–3946 and Mitchell et al. (2021) for multiple SNRs. Casanova et al. (2010) model accelerated CRs escaping SNR RX J1713.7–3946 in the hadronic and leptonic scenarios. Morphology maps of the γ -ray energy flux at 1 TeV were obtained using the distribution of the ambient gas for different diffusion conditions. Casanova et al. (2010) model the γ -ray morphology by utilising the LAB survey of HI and the Nanten survey of CO, which provides a detailed look into the distribution of γ -ray emission.

This work expands on our previous paper by predicting the morphology arising from the diffusive energy-dependent escape of CR protons and interaction with the surrounding ISM in the hadronic scenario. We make use of the spherically symmetric case for the isotropic transport equation from Aharonian & Atoyan (1996), assuming CR protons are accelerated by a single source and the energy-dependent diffusion coefficient is constant with position. The γ -ray emission is modelled across all pixels of the gas column density map from the Mopra $^{12}\text{CO}(1-0)$ survey and the Southern Galactic Plane Survey (SGPS) of HI for a wide range of parameters, to find the best combination of model parameters to match the observations. We present a first look at the 2D spatial morphology of γ -rays towards HESS J1804–216. This provides an important framework for understanding the region surrounding γ -ray sources, in particular the diffusive transport of particles from SNRs into the ISM.

2 DATA

The distribution of atomic hydrogen (HI) from the SGPS¹ (McClure-Griffiths et al. 2005) and molecular hydrogen, specifically $^{12}\text{CO}(1-0)$, from the Mopra radio telescope² are utilised. The Australia Telescope National Facility (ATNF) analysis software, LIVEDATA, GRIDZILLA, and MIRIAD in addition to custom IDL routines were used to process the data from Mopra (Burton et al. 2013; Braiding et al. 2018). Integrated emission maps were generated from the FITS cubes.

In this work, we use maps of total column density as these provide

¹ SGPS data can be found at https://www.atnf.csiro.au/research/HI/sgps/fits_files.html

² Published Mopra data can be found at <https://dataverse.harvard.edu/dataverse/harvard/>

the distribution of the total target material towards HESS J1804–216. The total hydrogen column density, N_{H} , is the sum of N_{HI} and $2N_{\text{H}_2}$, from SGPS HI observations and Mopra ^{12}CO (regridded to the SGPS HI pixel size of ~ 40 arcsec).

The two plausible counterparts of interest are SNR G8.7–0.1 and the progenitor SNR of PSR J1803–2137 which are at distances of 4.5 kpc (Hewitt & Yusef-Zadeh 2009) and 3.8 kpc (Briskin et al. 2006), respectively. SNR G8.7–0.1 has an age of 15–28 kyr (Finley & Oegelman 1994) and the progenitor SNR of PSR J1803–2137 has an age of 16 kyr (Briskin et al. 2006), assumed to be the same age as the pulsar it is attached to.

An 1720 MHz OH maser is indicative of interaction between SNRs and ISM clouds (Hewitt & Yusef-Zadeh 2009). Given the OH maser velocity of 36 km s^{-1} , we expect SNR G8.7–0.1 to be at a similar velocity. With use of the galactic rotation curve (GRC, Brand & Blitz 1993) and the distance to each SNR, the progenitor SNR of PSR J1803–2137 and SNR G8.7–0.1 are placed at a velocity of $\sim 25 \text{ km s}^{-1}$ and $\sim 35 \text{ km s}^{-1}$, respectively.

The velocity components are determined by taking the velocity of each counterpart as the mid-point of our range. If the velocity ranges chosen are too large, additional gas emission which is likely not connected to the source will be included. Due to local motions in the gas and the uncertainty of the GRC model, we estimate that the velocity bands should span 10 km s^{-1} . The position-velocity plots in Fig. A1 and Fig. A2 show that our defined velocity regions are reasonable as they do not include too much of the gas located in the galactic arms. Currently, the SGPS HI data (Fig. A2) does not reveal any HI voids making it hard to narrow down these velocity ranges further. Future HI surveys, such as the GASKAP HI survey (Dickey et al. 2013), will have a higher resolution and be more sensitive to voids and bubbles in the HI gas. Fig. 2 shows the total column density maps derived from SGPS HI and Mopra CO for Components 1 ($v_{\text{LSR}} = 20$ to 30 km s^{-1}) and 2 ($v_{\text{LSR}} = 30$ to 40 km s^{-1}).

The TeV γ -ray data used throughout this paper are from H.E.S.S.. Fig. 1 shows the γ -ray flux map above 1 TeV of HESS J1804–216 from the H.E.S.S. Galactic Plane Survey (HGPS, H. E. S. S. Collaboration et al. 2018a). The HGPS γ -ray flux maps are available as oversampled maps which are obtained by dividing the survey region into a grid of 0.02° , then summing all values within a circular radius of 0.1° for each grid point.

The spectral γ -ray data from Aharonian et al. (2006) is utilised, as this paper focussed on the TeV γ -ray sources in the inner part of the Galactic plane, including HESS J1804–216, providing a detailed look at the spectra and morphology of the TeV γ -ray observations. The Aharonian et al. (2006) and H. E. S. S. Collaboration et al. (2018a) data show good spectral matches as shown in Fig. C1. The Aharonian et al. (2006) data provides more spectral data points which will allow the spectral shape of our model to be compared with observations. The HESS J1804–216 spectral γ -ray observations from Aharonian et al. (2006) were extracted from a circular region of $\sim 0.36^\circ$ radius centred on HESS J1804–216 ($l = 8.4^\circ$, $b = -0.03^\circ$). We also make use of the spectral γ -ray data of 3FHL J1804.7–2144e from Ajello et al. (2017), extracted from a disk region of 0.38° (centred on $l = 8.4^\circ$, $b = -0.09^\circ$).

3 MODELLING

SNRs can be described as impulsive accelerators, in which CRs are accelerated by the SNR shock front, and escape into the ISM. We model the energy-dependent escape and subsequent diffusive transport of these particles using the solution to the isotropic diffusive

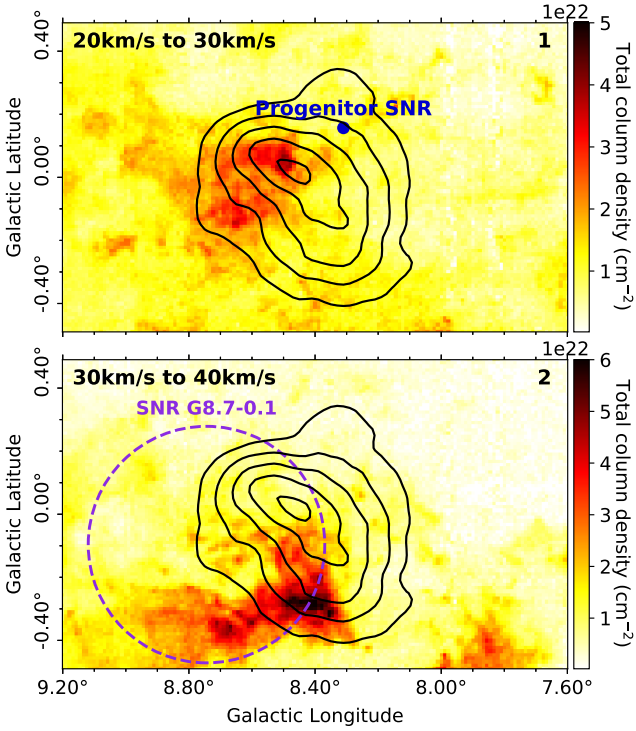


Figure 2. Total column density maps, $N_{\text{HI}} + 2N_{\text{H}_2}$, (cm^{-2}) towards HESS J1804–216, for gas components 1 and 2. The progenitor SNR of PSR J1803–2137 is indicated by the blue dot and the dashed purple circle indicates SNR G8.7–0.1. The TeV γ -ray emission from [H. E. S. S. Collaboration et al. \(2018a\)](#) is shown by the solid black contours (2×10^{-13} to $6 \times 10^{-13} \text{ cm}^{-2} \text{ s}^{-1}$ levels).

transport equation ([Aharonian & Atoyan 1996](#)). The injection of CRs is assumed to follow a power law, $E_p^{-\alpha}$, with a spectral index of α . Protons of different energies escape the accelerator at different times, where the higher energy protons leave the shock earlier than lower energy protons. Particles then diffuse through the ISM and interact to produce γ -rays. Where relevant, we assume either a Type Ia or Type II supernova explosion occurs with a total kinetic energy of E_{SN} , and an energy budget in CRs of $W_p = \eta E_{\text{SN}}$, where $\eta \leq 0.5$ ([Ackermann et al. 2013](#); [Berezhko & Völk 1997, 2000](#)).

3.1 Proton flux

The volume distribution of CRs, escaping from a shell, taking into account the time-dependent escape of protons of energy E_p is given by [equation \(1\)](#).

$$J_p(E_p, R, t) = N_0 E_p^{-\alpha} f_p(E_p, R, t) \text{ TeV}^{-1} \text{ cm}^{-3}, \quad (1)$$

where $f_p(E_p, R, t)$ is the probability density function (PDF) of protons, describing the probability of finding a particle of energy E_p at some distance from the accelerator, R . The time, t , is the time after the SNR explosion. As we are interested in the evolutionary state of the SNR, we will use $t = t_{\text{SNR}}$ in our model. The number density in our model is low ($n_{\text{H}} < 10^2 \text{ cm}^{-3}$) which leads to a high proton-proton cooling time, $\tau_{\text{pp}} \sim 6 \times 10^7 (n_{\text{H}}/\text{cm}^{-3})^{-1} \text{ yr}$. As we consider relatively young accelerators ($\tau_{\text{pp}} \gg t$, where $t < 100 \text{ kyr}$), we can neglect the cooling term in our model.

We assume the energy budget in CRs is the total energy of particles

with energies from $E_{p,\text{min}}$ to $E_{p,\text{max}}$, $W_p = N_0 \int_{E_{p,\text{min}}}^{E_{p,\text{max}}} E E^{-\alpha} dE$. From this definition we determine the normalisation factor, N_0 , where the maximum energy is, $E_{p,\text{max}}$ and the minimum energy is $E_{p,\text{min}} = 1 \text{ GeV}$.

We note that Equation 3 from [Aharonian & Atoyan \(1996\)](#) relates to particles released from a point source. Our model instead, describes the time-dependent release of particles from a shell, so a modification (explained shortly) to account for this is adopted. The PDF of CR protons of energy E_p is given by:

$$f_p(E_p, R, t) = \begin{cases} f_{\text{bubble}}(E_p, R, t) & E_p < E_{p,\text{esc}}, R < R_{\text{esc}} \\ f_{\text{dif}}(E_p, R, t) & E_p > E_{p,\text{esc}}, R > R_{\text{esc}} \\ 0 & \text{Otherwise} \end{cases} \quad (2)$$

The radius at which CR protons are released from the accelerator is given by [equation \(3\)](#) ([Reynolds 2008](#)).

$$R_{\text{esc}} = 0.31 \left(\frac{E_{\text{SN}}}{10^{51} \text{ erg}} \right)^{1/5} \left(\frac{n_0}{\text{cm}^{-3}} \right)^{-1/5} \left(\frac{t_{\text{esc}}}{\text{yr}} \right)^{2/5} \text{ pc}, \quad (3)$$

where n_0 is the ISM number density the SNR shock wave expands into ([Ptuskin & Zirakashvili 2005](#); [Reynolds 2008](#); [Ptuskin et al. 2010](#)). The escape time of CR protons is ([Gabici et al. 2009](#)):

$$t_{\text{esc}}(E_p) = t_{\text{sedov}} \left(\frac{E_p}{E_{p,\text{max}}} \right)^{-1/\delta_p}, \quad (4)$$

where $E_{p,\text{max}}$ are the most energetic particles present at the start of the Sedov-Taylor phase. The onset of the Sedov-Taylor phase, t_{sedov} , is defined by [equation \(B1\)](#).

The escape energy of protons is defined by rearranging [equation \(4\)](#) and setting $t_{\text{esc}} = t_{\text{SNR}}$:

$$E_{p,\text{esc}} = E_{p,\text{max}} \left(\frac{t_{\text{sedov}}}{t_{\text{SNR}}} \right)^{\delta_p}. \quad (5)$$

Particles at distance less than R_{esc} and with energy less than $E_{p,\text{esc}}$ are trapped inside a sphere, which we call the ‘bubble’. We assume that particles are uniformly distributed within this bubble, therefore the CR proton distribution can be described through:

$$f_{\text{bubble}}(E_p, R, t) = \frac{1}{(4/3)\pi R_{\text{esc}}^3}. \quad (6)$$

The PDF for diffused CR protons is given by ([Mitchell et al. 2021](#)):

$$f_{\text{dif}}(E_p, R, t) = \frac{f_0}{\pi^{3/2} R_{\text{dif}}^3} \exp\left(-\frac{(R - R_{\text{esc}})^2}{R_{\text{dif}}^2}\right). \quad (7)$$

We require our equation to be normalised, with a factor:

$$f_0 = \frac{\sqrt{\pi} R_{\text{dif}}^3}{(\sqrt{\pi} R_{\text{dif}}^2 + 2\sqrt{\pi} R_{\text{esc}}^2) |R_{\text{dif}}| + 4R_{\text{esc}} R_{\text{dif}}^2}. \quad (8)$$

The diffusion radius is

$$R_{\text{dif}} \equiv R_{\text{dif}}(E_p, t) = 2\sqrt{D(E_p)t'}, \quad (9)$$

where $t' = t - t_{\text{esc}}(E_p)$ represents the time the particles spend

in the ISM. The energy-dependent diffusion coefficient from Gabici et al. (2007) is used:

$$D(E_p) = \chi D_0 \left(\frac{E_p/\text{GeV}}{B/3\mu\text{G}} \right)^\delta, \quad (10)$$

where D_0 takes the Galactic average value of $3 \times 10^{27} \text{ cm}^2 \text{ s}^{-1}$ (Berezinskii et al. 1990), the diffusion suppression factor is χ and the index of diffusion is δ . The magnetic field is taken as a constant value of $B = B_0 = 10 \mu\text{G}$ as the average number density of the ISM surrounding HESS J1804–216 is low ($n_{\text{H}} < 300 \text{ cm}^{-3}$, Crutcher et al. 2010). At low density, the magnetic field does not scale with density, due to diffuse clouds (low density) being assembled by motions along the magnetic field. The estimates from Zeeman splitting are also neglected at low density, as they are only significant for the dense ISM. This low magnetic field means particles in our model diffuse faster, as the diffusion coefficient increases.

3.2 Gamma-ray flux

The differential γ -ray flux ($\text{TeV}^{-1} \text{ cm}^{-2} \text{ s}^{-1}$) for the energy interval ($E_\gamma, E_\gamma + dE_\gamma$) at position R and time t is computed through (Kelner et al. 2006):

$$\mathcal{F}_\gamma(E_\gamma, R, t) = \frac{N_{\text{H}} A}{4\pi D^2} c \int_{E_\gamma}^{\infty} \sigma_{\text{pp}}(E_p) J_{\text{p}}(E_p, R, t) F_\gamma \left(\frac{E_\gamma}{E_p}, E_\gamma \right) \frac{dE_p}{E_p}, \quad (11)$$

where A and N_{H} are the area, and total hydrogen column density of the region of interest, D is the distance from Earth to the accelerator and c is the speed of light. The inelastic cross section of proton-proton interactions is σ_{pp} (equation (B2)) and F_γ is the number of photons per collision given by equation (B3).

4 METHODOLOGY

We calculate the volume distribution of CR protons using equation (1) at every pixel in the total column density map, for a range of proton energies. The predicted 3D γ -ray map is created with the z-axis being γ -ray energy, via equation (11), by combining the proton map with the ISM distribution. The resulting γ -ray ‘cube’ is used to extract spectra and integrated flux maps. Fig. 3 shows a schematic of the model.

Our model has a range of parameters. Multiple parameters have a similar effect on the model, for example, χ and δ , which both effect the diffusion coefficient, which leads to a redundancy in our model solution. Due to this, we cannot perform a purely quantitative optimisation across the entire parameter space. Instead, we perform a systematic grid search over a range of model parameters, in which each combination is modelled, based on typical values from literature, as discussed below and compare these models to γ -ray observations. We calculate metrics to quantify the agreement of GeV-TeV observations with our model. To compare the modelled morphology to the HGPS observations, the oversampling method from H.E.S.S. is applied, as described in Section 2.

The spatial model of γ -rays is largely biased by the bubble component because the accelerators considered here lie within the extension of the γ -ray source. Therefore, we use the spectral model to determine the best matching model. We use the following metric for the

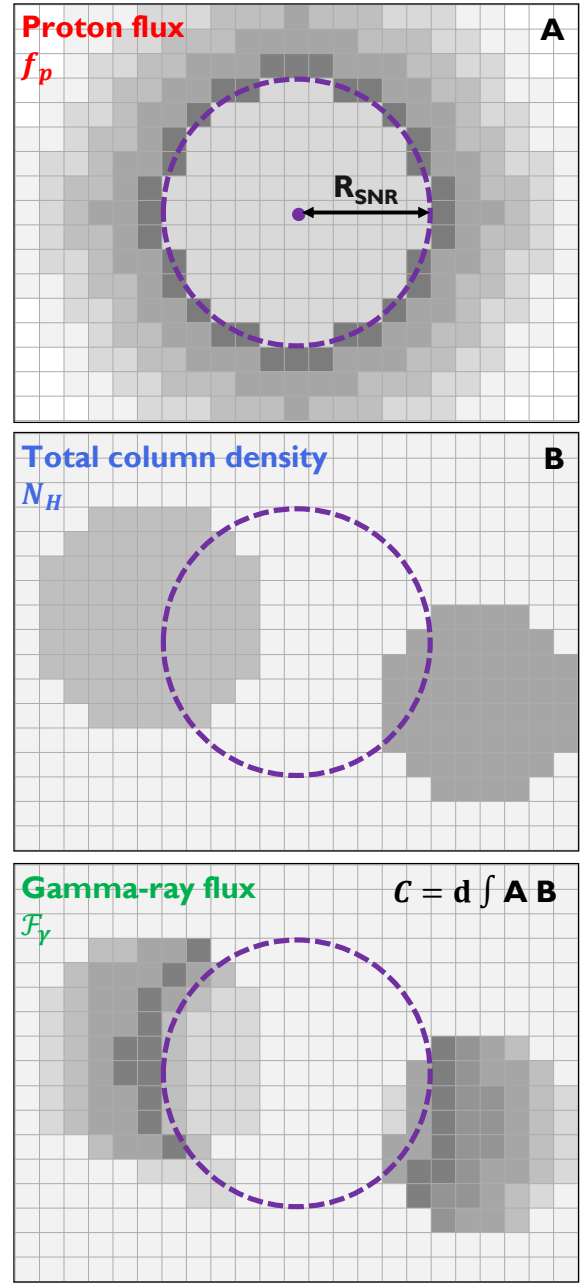


Figure 3. Schematic illustrating our model. *Top*: example distribution of CR protons (equation (2)). *Middle*: example distribution of the total column density gas. *Bottom*: example distribution of γ -ray flux (equation (11)) by integrating over the top and middle panels with some constant.

spectral optimisation:

$$\frac{\chi^2}{m} = \left(\sum_i \frac{(O_i - F_i)^2}{G_i^2} \right) \frac{1}{m}, \quad (12)$$

where O_i is the observed flux, F_i is the model flux, G_i is the uncertainty in the observations, i denotes each data point and m is the number of data points. For testing the spatial agreement, we integrated the γ -ray cube from 1 TeV to 100 TeV to compare to the flux map from H. E. S. S. Collaboration et al. (2018a). As a metric for the spatial model we calculate the standard deviation, S (equation (13)),

of the residuals but exclude the bubble region as we do not model the distribution of particles in detail there.

$$S = \frac{\sum_i (R_i - \mu)^2}{N} \quad (13)$$

Here $R_i = O_i - F_i$ is the residual from the spatial morphology map (residual maps are provided in the supplementary material) for the i^{th} pixel, μ is the mean and N is the number of pixels in the residual map.

Model parameter variation

SNRs are thought to be the main source of CRs for energies below the knee of the CR spectrum (at PeV energies, [Lucek & Bell 2000](#)). We define the maximum energy of protons, $E_{p,\text{max}}$, at the start of the Sedov phase to be either 1 PeV or 5 PeV ([Gabici et al. 2009](#)), for [equations \(4\) and \(5\)](#) and in the normalisation factor, N_0 . The energy budget, W_p , is a free parameter which is optimised by minimising the residual between the observations and model spectra. From diffusive shock acceleration theory, we expect a power law with a spectral index of $\alpha \approx 2$ ([Malkov & Drury 2001](#)). Therefore, we vary the spectral index from 1.8 to 2.4 in our model.

The factor χ varies from 0.001 to 1, the lower limit ($\chi = 0.001$) is potentially applicable to the dense regions of interstellar gas that the CRs may diffuse through, and the upper limit is taken from various observations (see [Feijen et al. 2020](#), and references therein). Typically, δ varies from 0.3 to 0.7 ([Berezinskii et al. 1990](#)) to allow for a range of turbulent spectra to be investigated. Here 0.3 corresponds to Kolmogorov turbulence (indicating slower diffusion), 0.5 indicates Kraichnan turbulence ([Strong et al. 2007](#)) and 0.7 is consistent with a good fit to the Boron to Carbon ratio measurements.

In [equation \(4\)](#), δ_p describes the energy-dependent release of CRs. The lower limit is taken to be 1/5 which is for a simple stationary particle and the upper limit is taken to be 2.5 ([Ptuskin & Zirakashvili 2005](#); [Celli et al. 2019](#); [Gabici et al. 2009](#)). For the Sedov time in [equation \(B1\)](#) we take the typical mass and energy values for different supernovae types. We find for Type Ia, where $M_{\text{ej}} = 1M_{\odot}$ ([Ptuskin & Zirakashvili 2005](#)) and $E_{\text{SN}} = 10^{51}$ erg, the Sedov time is $t_{\text{sedov}} \sim 230\text{yr}$. For Type II, where $M_{\text{ej}} = 10M_{\odot}$ and $M_{\text{ej}} = 20M_{\odot}$ ([Heger et al. 2003](#)) with $E_{\text{SN}} = 10^{51}$ erg, the Sedov time is $t_{\text{sedov}} \sim 1600\text{yr}$ and $t_{\text{sedov}} \sim 2850\text{yr}$, respectively. Type II can also have a higher total kinetic energy ([Nomoto et al. 2004](#)) of $E_{\text{SN}} = 10^{52}$ erg for $M_{\text{ej}} = 10M_{\odot}$ and $M_{\text{ej}} = 20M_{\odot}$, where the Sedov time is $t_{\text{sedov}} \sim 500\text{yr}$ and $t_{\text{sedov}} \sim 900\text{yr}$, respectively.

We expect n_0 , from [equation \(3\)](#), to be a small value as it is close to ‘SNR birth’ before the shock wave has interacted with the gas. If we know the age, t_{SNR} , and radius, R_{SNR} , of the SNR we estimate n_0 by rearranging [equation \(3\)](#):

$$n_0 = \left[\frac{0.31\text{pc}}{R_{\text{SNR}}} \left(\frac{E_{\text{SN}}}{10^{51}\text{erg}} \right)^{1/5} \left(\frac{t_{\text{SNR}}}{\text{yr}} \right)^{2/5} \right]^5 \text{cm}^{-3}. \quad (14)$$

If R_{SNR} is not known, n_0 takes on values from 0.1 to 20cm^{-3} . The model parameters discussed are summarised in [Table 1](#).

5 BEST MATCHING MODELS

The following section considers the best matching models for each accelerator, based on the parameter space and minimising the spectral and spatial criteria ([equations \(12\) and \(13\)](#), respectively), as

Table 1. Model parameters with their discrete values. The spectral index is α , the diffusion suppression factor and the index of diffusion coefficient are given by χ and δ , respectively. The maximum CR proton energy is $E_{p,\text{max}}$ and δ_p describes the energy-dependent release of CRs. E_{SN} is the kinetic energy released at the supernova explosion and M_{ej} is the mass of the ejecta.

Parameter	Values
α	1.8, 2.0, 2.2, 2.4
χ	0.001, 0.01, 0.1, 1.0
δ	0.3, 0.4, 0.5, 0.6, 0.7
δ_p	0.2, 1.4, 2.5
$E_{p,\text{max}}$	1, 5 PeV
M_{ej} and E_{SN}	$1M_{\odot}$ and 10^{51} erg (Type Ia) $10M_{\odot}$, $20M_{\odot}$ and 10^{51} erg (Type II) $10M_{\odot}$, $20M_{\odot}$ and 10^{52} erg (Type II)
n_0^*	0.1, 1, 10, 20cm^{-3}

* For progenitor SNR of PSR J1803–2137

described in [Section 4](#). Specifically, the 5 best matching spectral models are chosen for each accelerator.

5.1 SNR G8.7–0.1

SNR G8.7–0.1 is believed to be contained in Component 2 ($v_{\text{lsr}} = 30$ to 40km s^{-1}). We test the various model parameters for both Type Ia and Type II supernovae for both suggested ages of SNR G8.7–0.1, 15 kyr and 28 kyr, the results shown here are the closest matching spectra to the observations. [Tables D1 and D2](#) show the 5 best matching spectral models with their ranking parameters for the spectral and spatial models, χ^2/m and S respectively.

The 5 best matching models for SNR G8.7–0.1 for each age show a range of χ and δ values. Typically a moderately slow diffusion with $\chi = 0.001$ or 0.01 is seen, which is consistent with other studies in which the diffusion coefficient is suppressed ([Gabici et al. 2007](#); [Li & Chen 2010](#); [Giuliani et al. 2010](#)). The index for the energy-dependent release of CRs, δ_p , takes on values of 1.4 or 2.5. A mixture of the $E_{p,\text{max}}$ values are present. For SNR G8.7–0.1 we find both a Type Ia SN and Type II SN, match the γ -ray spectra well for both ages of this accelerator. The escape energy of protons, $E_{p,\text{esc}}$, in [Figs. 4 and 5](#) are 15.8 TeV and 6.2 TeV respectively. CR protons with energy lower than $E_{p,\text{esc}}$ are still confined in the bubble, however higher energy particles have escaped. This is shown by splitting the spectra into its bubble and diffused components as depicted in the top panels of [Figs. 4 and 5](#).

For our best matching models, [Figs. 4 and 5](#), the spectra tend to match well at low energies. The escape energies for these spectra are quite high, therefore the model spectra are largely dominated by the bubble component. This is seen at higher energies, where the model begins to deviate from the observations, particularly in [Fig. 4](#).

The spatial morphology above 1 TeV cannot explain the γ -ray emission from HESS J1804–216. One contributing factor is the bubble component encompassing a large area of the H.E.S.S. source. The simulated γ -ray emission shows a peak toward the northern edge of HESS J1804–216 and a lack of γ -ray emission towards the western TeV peak of HESS J1804–216. Simulated γ -ray emission is also present at the outer western edge of SNR G8.7–0.1 for both ages, which is not present in the observations from H.E.S.S.. The closest TeV γ -ray source from the HGPS is HESS J1808–204, which is an extended source located at $l = 10.01$, $b = -0.24$, which is not

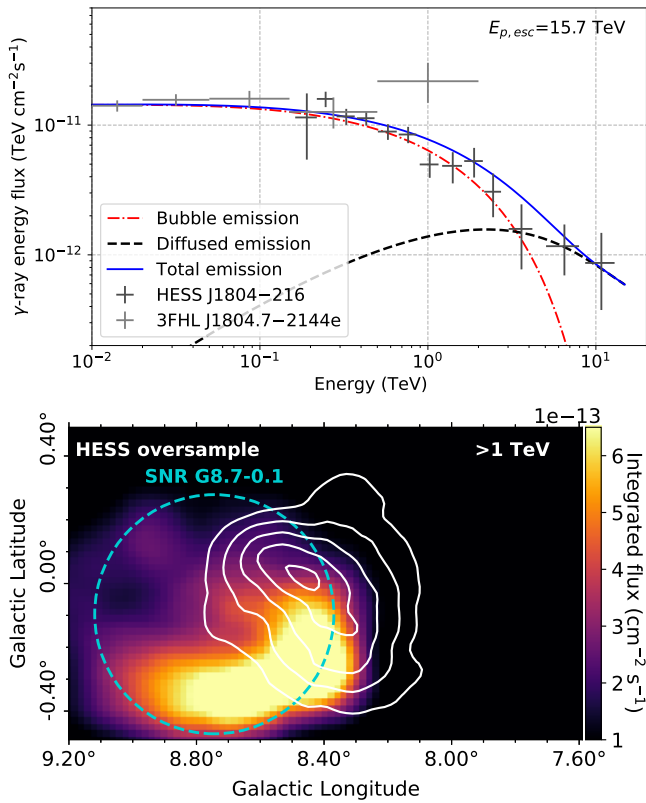


Figure 4. Best matching spectral and spatial model (G4a) for SNR G8.7–0.1 with an age of 15 kyr. *Top*: γ -ray spectral model shown in blue. The diffused and bubble spectra are shown by the dashed black curve and dot-dashed red curve, respectively, with HESS J1804–216 observations in dark gray and 3FHL J1804.7–2144e observations in light gray. *Bottom*: γ -ray flux map above 1 TeV towards HESS J1804–216. The escape radius, R_{esc} , is shown by cyan dashed circle. The TeV γ -ray emission from [H. E. S. S. Collaboration et al. \(2018a\)](#) shown by the solid white contours (2×10^{-13} to $6 \times 10^{-13} \text{ cm}^{-2} \text{ s}^{-1}$ levels). The lower limit of the colorbar is set to $10^{-13} \text{ cm}^{-2} \text{ s}^{-1}$ to exclude any emission below the sensitivity of H.E.S.S.. Model parameters: $\alpha = 2.0$, $\chi = 0.01$, $\delta = 0.6$, $\delta_p = 2.5$, $E_{p,\text{max}} = 1 \text{ PeV}$, Type II SN, $E_{p,\text{esc}} = 15.8 \text{ TeV}$. For the spectral model $\chi^2/m = 1.1$.

close enough to SNR G8.7–0.1 to provide the γ -ray emission at this position.

5.2 Progenitor SNR of PSR J1803–2137

The progenitor SNR is assumed to have an age of 16 kyr, as per the age of PSR J1803–2137, and is placed at the birth position of PSR J1803–2137 as shown in [Fig. 1](#). The progenitor SNR is believed to be in Component 1 ($v_{\text{lsr}} = 20$ to 30 km s^{-1}). We test a range of combinations of model parameters for a core-collapse supernova, as a pulsar is attached to the system. The 5 best matching spectral models with their ranking parameters for the spectral and spatial models, χ^2/m and S respectively, are shown in [Table D3](#).

[Table D3](#) shows the 5 best matching spectral models typically have a spectral index of $\alpha = 1.8$, with $\chi = 0.001$ or 0.01 and a range of δ . Similarly to SNR G8.7–0.1, this indicates moderately slow diffusion of particles. Both values of the maximum energy, $E_{p,\text{max}}$, are present and n_0 takes on all values in the parameter space. The total kinetic energy, E_{SN} , is typically the higher value from our parameter space of 10^{52} erg , with the ejecta mass being either $10M_{\odot}$ or $20M_{\odot}$. The

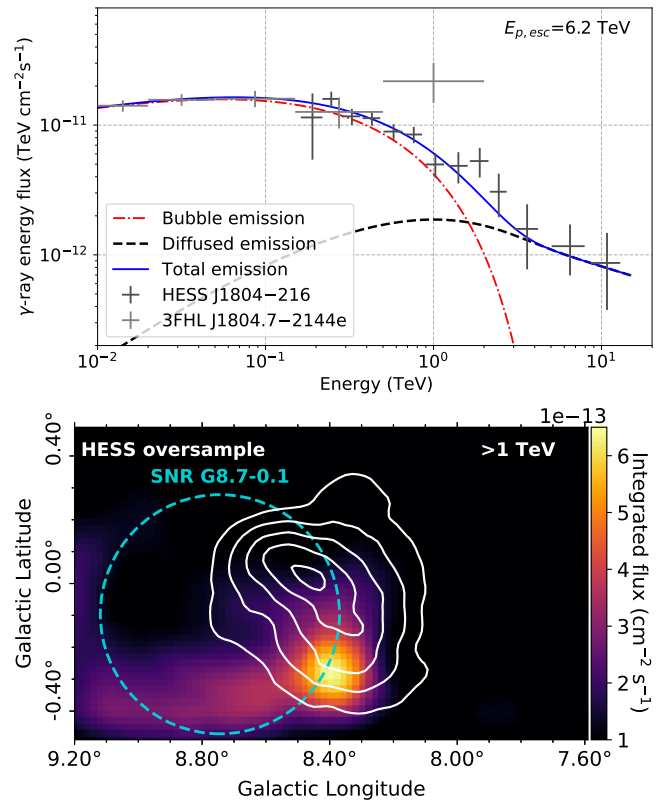


Figure 5. Best matching spectral and spatial model (G2b) for SNR G8.7–0.1 with an age of 28 kyr. *Top*: γ -ray spectral model shown in blue. The diffused and bubble spectra are shown by the dashed black curve and dot-dashed red curve, respectively, with HESS J1804–216 observations in dark gray and 3FHL J1804.7–2144e observations in light gray. *Bottom*: γ -ray flux map above 1 TeV towards HESS J1804–216. The escape radius, R_{esc} , is shown by cyan dashed circle. The TeV γ -ray emission from [H. E. S. S. Collaboration et al. \(2018a\)](#) shown by the solid white contours (2×10^{-13} to $6 \times 10^{-13} \text{ cm}^{-2} \text{ s}^{-1}$ levels). Model parameters: $\alpha = 1.8$, $\chi = 0.1$, $\delta = 0.4$, $\delta_p = 1.4$, $E_{p,\text{max}} = 5 \text{ PeV}$, Type Ia SN, $E_{p,\text{esc}} = 6.2 \text{ TeV}$. For the spectral model $\chi^2/m = 0.8$.

index for the energy-dependent release of CRs $\delta_p = 2.5$, the highest value chosen in our parameter space. The escape energy for the top model is $E_{p,\text{esc}} = 3.8 \text{ TeV}$, therefore some particles are still trapped in the bubble and some have diffused, this can be seen in the spectral components in [Fig. 6](#).

For this accelerator, both the spectral and spatial morphology match the observations well. The modelled integrated γ -ray map peaks towards the northern TeV peak of HESS J1804–216 from [H. E. S. S. Collaboration et al. \(2018a\)](#). There is weaker modelled γ -ray emission overlapping the entire γ -ray source and a lack of modelled emission outside the HESS J1804–216 region. No strong γ -ray emission is present outside HESS J1804–216 unlike with SNR G8.7–0.1. However, parts of the morphology do not match well due to the bubble component and the lack of γ -ray emission in the southern and eastern edges of HESS J1804–216.

6 DISCUSSION

In the previous section we compared the model emission with observational γ -ray emission above 1 TeV. [Fig. 17](#) from [Aharonian et al.](#)

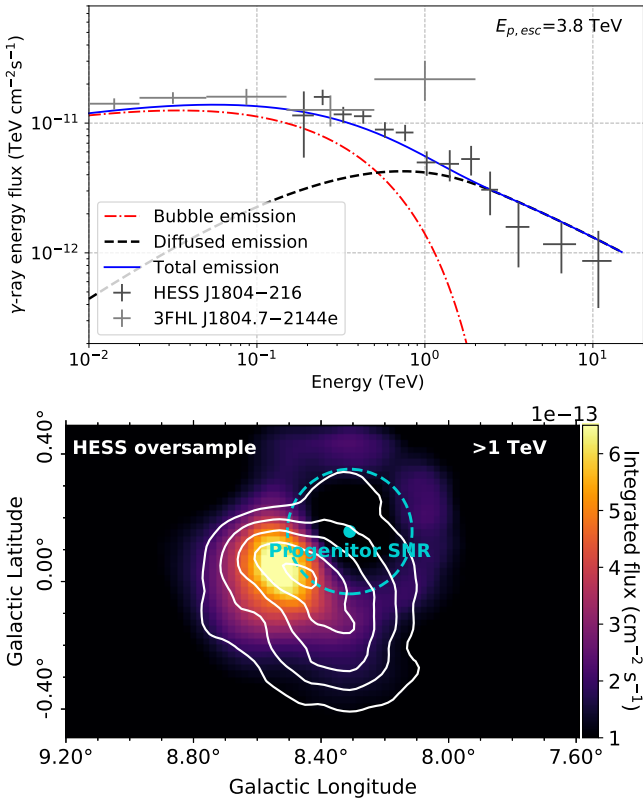


Figure 6. Best matching spectral and spatial model (P1) for the progenitor SNR of PSR J1803–2137. *Top:* γ -ray spectral model shown in blue. The diffused and bubble spectra are shown by the dashed black curve and dot-dashed red curve, respectively, with HESS J1804–216 observations in dark gray and 3FHL J1804.7–2144e observations in light gray. *Bottom:* γ -ray flux map above 1 TeV towards HESS J1804–216. The progenitor SNR of PSR J1803–2137 is indicated by the cyan dot and the escape radius, R_{esc} , is shown by cyan dashed circle. The TeV γ -ray emission from H. E. S. S. Collaboration et al. (2018a) shown by the solid white contours (2×10^{-13} to $6 \times 10^{-13} \text{ cm}^{-2} \text{ s}^{-1}$ levels). Model parameters: $\alpha = 1.8$, $\chi = 0.1$, $\delta = 0.4$, $\delta_p = 1.4$, $E_{p,\text{max}} = 5 \text{ PeV}$, Type Ia SN, $E_{p,\text{esc}} = 6.2 \text{ TeV}$. For the spectral model $\chi^2/m = 0.8$.

(2006) shows the morphology of HESS J1804–216 above 0.2 TeV, which is similar to the integrated flux morphology above 1 TeV in Fig. 1 (H. E. S. S. Collaboration et al. 2018a). Extensions of both HESS J1804–216 and 3FHL J1804.7–2144e overlap (Fig. 1). To probe the effects of the bubble and diffused components we look at the γ -ray emission in different energy bands: $E_\gamma=10\text{--}100 \text{ GeV}$, $E_\gamma=0.1\text{--}1 \text{ TeV}$, $E_\gamma=1\text{--}10 \text{ TeV}$, and $E_\gamma=10\text{--}100 \text{ TeV}$.

The morphology of the different energy bands for the SNR G8.7–0.1 accelerator show that the bubble component provides stronger γ -ray emission compared to the diffused component (as shown in Figs. 7 and 8). At higher energies ($E_\gamma=1\text{--}10 \text{ TeV}$, and $E_\gamma=10\text{--}100 \text{ TeV}$) the model exhibits strong emission towards the southern edge of HESS J1804–216, which does not overlap with the TeV peak. In comparing the four energy bands to morphology of HESS J1804–216, it is clear the morphology is quite different.

Fig. 9 shows the morphology from different energy bands for the best model of the progenitor SNR. The bubble tends to dominate at the best two lower energy bands ($E_\gamma=10\text{--}100 \text{ GeV}$ and $E_\gamma=0.1\text{--}1 \text{ TeV}$), with strong emission towards the pulsar birth position. The two higher energy bands ($E_\gamma=1\text{--}10 \text{ TeV}$ and $E_\gamma=10\text{--}100 \text{ TeV}$) show the γ -ray

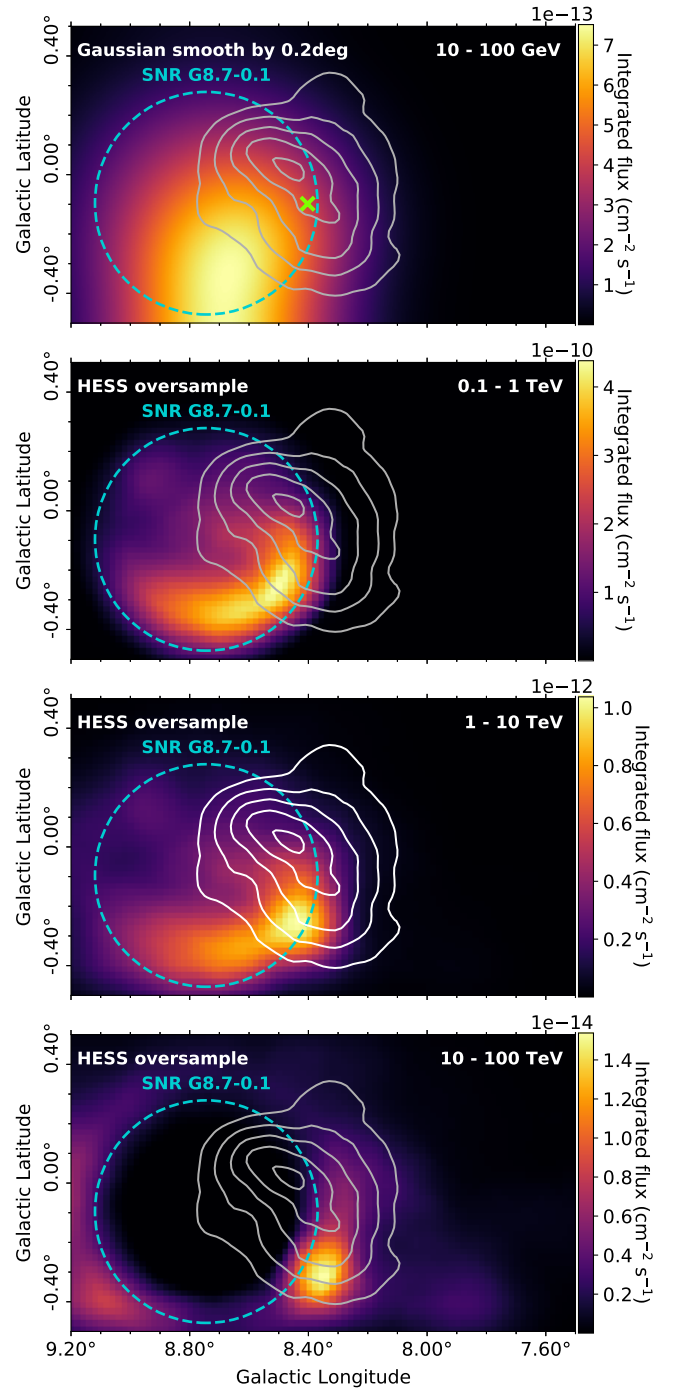


Figure 7. γ -ray flux maps for various energy bands towards HESS J1804–216 for the best matching model (G4a) for SNR G8.7–0.1 with an age of 15 kyr. The escape radius, R_{esc} , is shown by cyan dashed circle. The green cross indicates the centroid of 3FHL J1804.7–2144e. The first energy band ($E_\gamma=10\text{--}100 \text{ GeV}$) corresponds to energies detected by *Fermi*-LAT so is smoothed using the *Fermi*-LAT PSF of $\sim 0.2^\circ$ above 10 GeV (Ackermann et al. 2017). The other energy bands are oversampled using the H.E.S.S. method described in Section 2. The TeV γ -ray emission above 1 TeV from H. E. S. S. Collaboration et al. (2018a) is shown by the solid white contours in the third panel (2×10^{-13} to $6 \times 10^{-13} \text{ cm}^{-2} \text{ s}^{-1}$ levels) and by grey contours in the other panels as a reference for where the γ -ray emission is expected. Model parameters as described in Fig. 4.

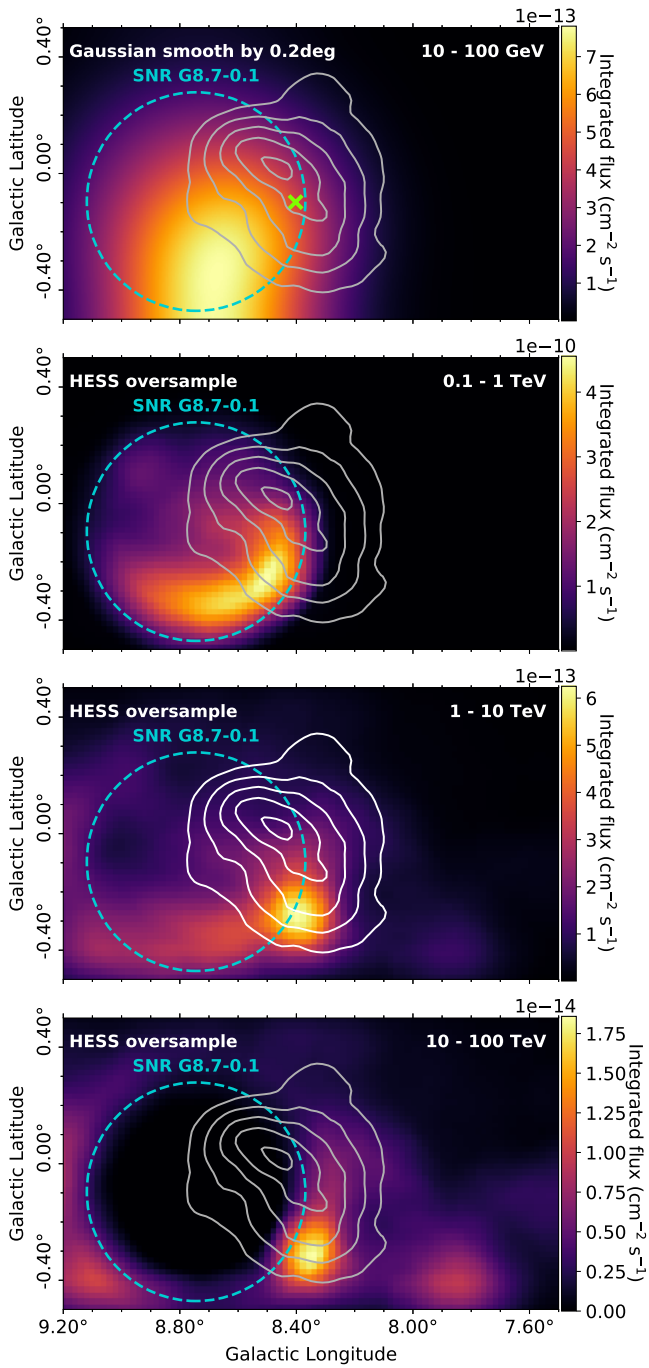


Figure 8. γ -ray flux maps for various energy bands towards HESS J1804–216 for the best matching model (G2b) for SNR G8.7–0.1 with an age of 28 kyr. The escape radius, R_{esc} , is shown by cyan dashed circle. The green cross indicates the centroid of 3FHL J1804.7–2144e. The solid white/grey contours are as described in Fig. 7. Model parameters as described in Fig. 5.

peak moves away from the pulsar position and closer to the TeV γ -ray peak from HGPS. The emission in these bands becomes diffusion-dominated with extended emission outside the bubble.

Overall, the γ -ray emission in the lower energy bands of Figs. 7 to 9 are dominated by the bubble component as the particles have energy less than the escape energy, so are still confined to the bubble region. However, above 1 TeV the diffused component becomes dom-

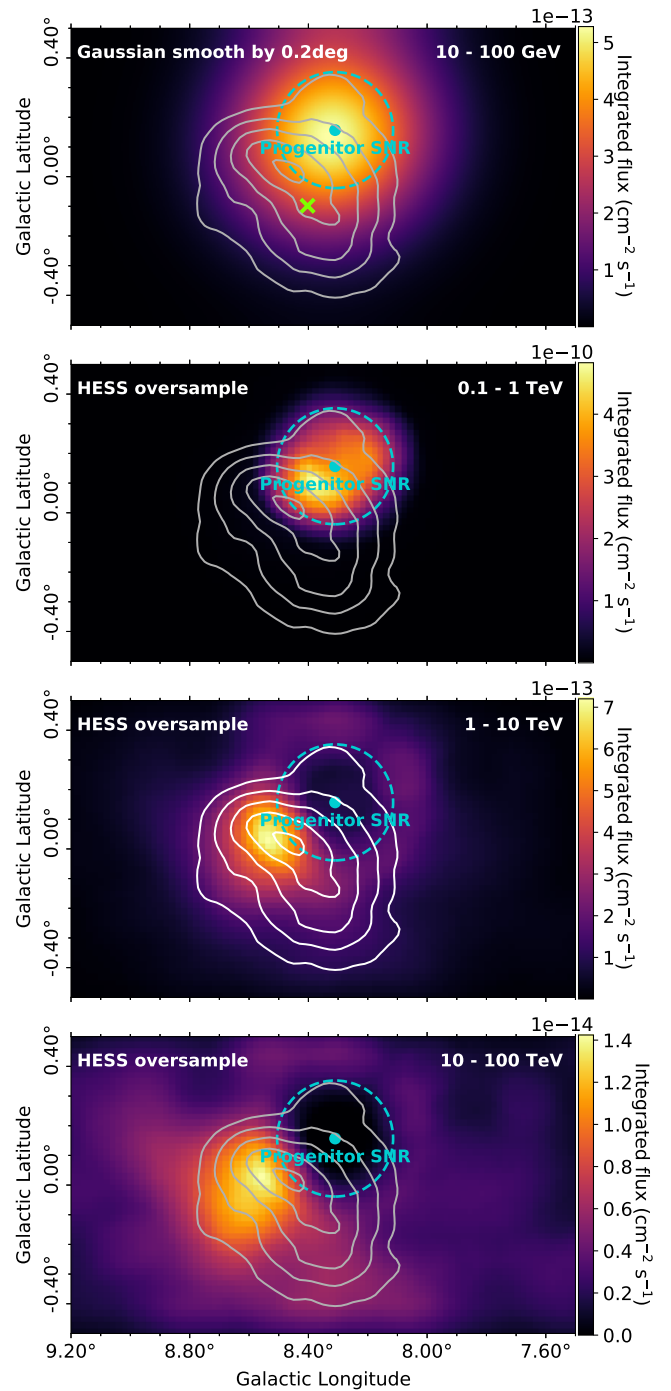


Figure 9. γ -ray flux maps for various energy bands towards HESS J1804–216 for the best matching model (P1) for the progenitor SNR of PSR J1803–2137. The escape radius, R_{esc} , is shown by cyan dashed circle. The green cross indicates the centroid of 3FHL J1804.7–2144e. The solid white/grey contours are as described in Fig. 7. Model parameters as described in Fig. 6.

inant. The morphology of the lower energy band can be compared with the spatial morphology of *Fermi*-LAT observations. However, *Fermi*-LAT has poor resolution (with a PSF of 0.2° above 10 GeV), so the spatial map from *Fermi*-LAT observations is described only by a circular region. Therefore, we can only compare the model morphology with the position and extent of 3FHL J1804.7–2144e (seen

in Fig. 1). For each accelerator model the peak of γ -ray emission is offset from the 3FHL catalogue position (by up to 0.4°).

There are a number of known limitations in our model. These arise from:

- (i) 2D propagation of CR protons
- (ii) 2D arrangement of the ISM
- (iii) Uniform distribution of CRs inside bubble
- (iv) Simple assumption of ISM inside bubble
- (v) Spherical uniformity of the SNR evolution

The main limitation comes from assuming a 2D geometry for the proton model in addition to the accelerators lying within the γ -ray source. This 2D approach to modelling the γ -rays has previously been implemented e.g. Casanova et al. (2010), in which the accelerator is further away from the γ -ray source. In our model, we have a special case in which both accelerators lie within the extension of the γ -ray source. As we do not model the diffusion inside the bubble component, our results are biased. In our 2D proton model, we do not consider particles diffusing along our line of sight, therefore we are not taking into account the emission foreground/background to the SNR bubble. This makes reconciling the morphology inside the bubble with the observations difficult and is the reason we do not use the spatial criterion (equation (13)) to test which model performs best.

Another limitation comes from the assumptions regarding the ISM surrounding HESS J1804–216. We assume a 2D model in which the brightness temperature gas cube is integrated over to obtain a total column density map. By using the column density map we assume that all gas we integrated over is interacting with the CRs. Due to this, we could be including gas that is foreground and/or background to the accelerator, which may not be physically able to interact with the accelerated protons. This effect is more prominent for the bubble component which has radius $R_{\text{esc}} \sim 30$ pc compared to the entire column which is integrated over 10 km s^{-1} corresponding to ~ 800 pc from the GRC. Our model could therefore be over predicting the bubble component.

One of the largest uncertainties in our model comes from the distribution of CRs and density of the ISM inside the bubble. We assume the CRs are uniformly distributed in the bubble (see e.g. Zirakashvili & Aharonian 2010), however realistically the particle distribution is more complex, with CRs likely accumulating in the shock region (i.e. the expanding SNR shell), as explored by some theoretical studies (Ptuskin & Zirakashvili 2005; Celli et al. 2019; Brose et al. 2020). They suggest the CR distribution can be ‘shell’ brightened. From diffusive shock acceleration theory, it is possible that the shocked ISM could be ~ 4 times denser than the unshocked gas (Reynolds 2008), according to the expected shock compression factor. Furthermore, it is possible for some of the ISM here to be dissociated by the SNR shock, thereby reducing the density (Fukui et al. 2003; Sano et al. 2020).

For limitation (v) we assume a constant number density for the SNR evolution (n_0 , in equation (3)), leading to spherical uniformity of the particle escape radius. The escape energy is dependent upon δ_p , which describes the energy dependent release of CRs, which can also effect the evolution of the SNR. A future version of the model would involve tracing the evolution of the shock in closer detail, including the escape radius as it changed with ISM density.

7 CONCLUSIONS

We developed a model to investigate the distribution of γ -rays towards HESS J1804–216 for two SNRs in the hadronic scenario. This is a first attempt to model the morphology of γ -rays towards HESS J1804–216. γ -ray spectra and morphology maps of SNR G8.7–0.1 and the progenitor SNR of PSR J1803–2137 were generated for a range of model parameters and compared to observations to gain an understanding of the origin of HESS J1804–216. It was found that the progenitor SNR is the most promising candidate to be creating the TeV γ -rays, however, we are limited by the bubble component. The modelled γ -ray morphology from SNR G8.7–0.1 does not match the γ -ray morphology from observations well, therefore it is either only a minor contributor or does not contribute to the observed γ -ray emission.

The γ -ray observatory CTA (Cherenkov Telescope Array) aims to improve the current measurements from other Imaging Atmospheric Cherenkov Telescope. More detailed features in the morphology may be resolved with CTA, which will provide unprecedented angular resolution and sensitivity. The angular resolution of CTA will reach a few arcmins, comparable to the angular resolution of the Mopra radio telescope, which is utilised for our gas measurements. Here we compare the best matching model of the progenitor SNR of PSR J1803–2137 (P1) for three different angular resolutions using different oversampling settings for each instrument. The original model (no oversampling, same resolution as the gas maps), the H.E.S.S. oversample (radius= 0.1° with a grid size of 0.02°) and the expected CTA oversample (radius= 0.03° with a grid size of 0.01° , as per the expected angular resolution from CTA Consortium et al. 2018) maps are shown in Fig. 10.

Fig. 10 shows that the oversampling of CTA (bottom panel) is able to resolve features, comparable to the gas map resolution (middle panel with no oversample), meaning the morphology can be further probed with CTA.

Our model provides a good framework for future studies, including insight into what parameters are required. A numerical approach in 3D could be used to more precisely model the particles injected, for each time step. This involves tracing the accelerated particles as they propagate and subsequently interact with the ISM, based on the magnetic field and diffusion parameters of each grid point in the model, hence it is a very computationally expensive approach.

For our model, we currently consider an impulsive injection of particles from the accelerator for the hadronic scenario. Mature aged SNRs may also produce γ -rays leptonically through the inverse-Compton effect (e.g. Araya & Frutos 2012; Devin et al. 2018; Fukui et al. 2021). To finally confirm the accelerator of HESS J1804–216, we need to explore the leptonic scenario, assuming the SNR is accelerating electrons which may contribute to the TeV γ -ray emission as discussed by Ajello et al. (2012); Liu et al. (2019). TeV emission from a PWNe is a reasonable assumption due to the turn-over in the GeV/TeV spectrum, which could be caused by cooling effects of electrons. Along with this, a continuous acceleration scenario should be investigated for both leptonic (typical of PWNe) and hadronic origins. Our model predicts an energy-dependent morphology, largely due to the bubble component, which is not implied by the GeV/TeV observations. Future work will include an energy-dependent morphology study of the H.E.S.S. data, to investigate this further. A dedicated study of the *Fermi*-LAT data could also help to resolve the morphology of γ -rays at lower energies, in addition to the use of CTA in the future. These methods will hopefully help reveal the nature of HESS J1804–216.

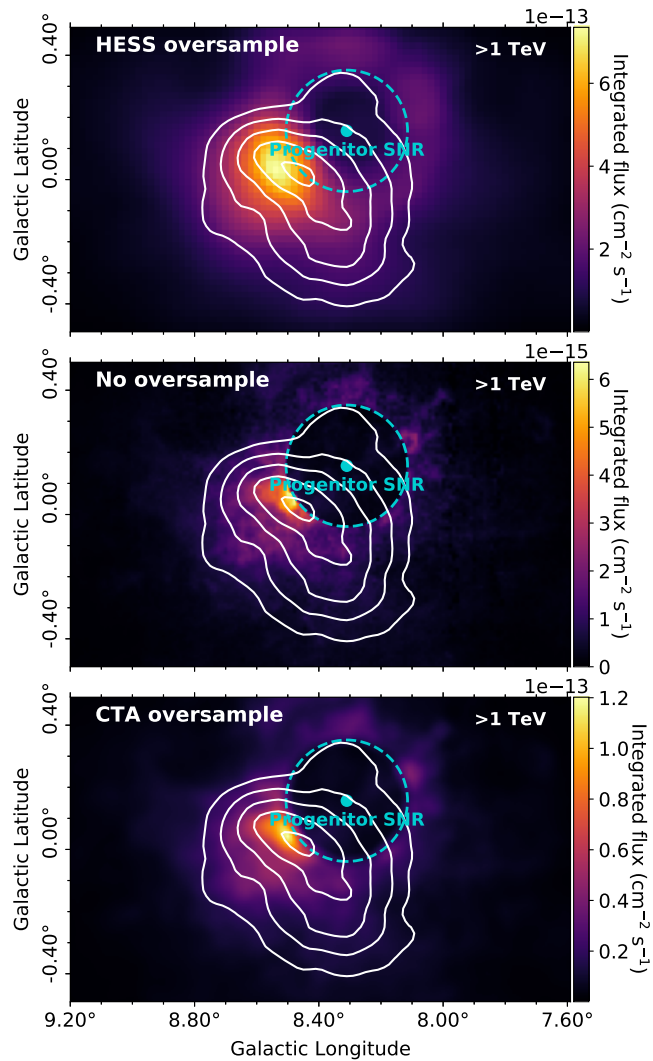


Figure 10. γ -ray flux maps above 1 TeV towards HESS J1804–216 with the progenitor SNR of PSR J1803–2137 as the accelerator (for the top model, P1). The TeV γ -ray emission from H. E. S. S. Collaboration et al. (2018a) shown by the solid white contours (2×10^{-13} to $6 \times 10^{-13} \text{ cm}^{-2} \text{ s}^{-1}$ levels). *Top:* Map oversampled with H.E.S.S. factor of radius= 0.1° with grid size of 0.02° . *Middle:* Map not oversampled, with same resolution as gas map. *Bottom:* Map oversampled with CTA factor of radius= 0.03° with grid size of 0.01° .

ACKNOWLEDGEMENTS

The Mopra telescope is part of the ATNF which is funded by the Australian Government for operation as a National Facility managed by CSIRO (Commonwealth Scientific and Industrial Research Organisation). Support for observations were provided by the University of New South Wales and the University of Adelaide. K.F. acknowledges support through the provision of Australian Government Research Training Program Scholarship.

DATA AVAILABILITY

The data underlying this article are available on the MopraGam website at <http://www.physics.adelaide.edu.au/astrophysics/MopraGam/>. Other datasets were derived from

sources in the public domain: HGPS at <https://www.mpi-hd.mpg.de/hfm/HESS/hgps/> and SGPS at https://www.atnf.csiro.au/research/HI/sgps/fits_files.html.

References

- Ackermann M., et al., 2013, *Science*, **339**, 807
 Ackermann M., et al., 2017, *ApJ*, **843**, 139
 Aharonian F. A., Atoyan A. M., 1996, *A&A*, **309**, 917
 Aharonian F., et al., 2006, *ApJ*, **636**, 777
 Ajello M., et al., 2012, *ApJ*, **744**, 80
 Ajello M., et al., 2017, *ApJS*, **232**, 18
 Araya M., Frutos F., 2012, *MNRAS*, **425**, 2810
 Berezhko E. G., Völk H. J., 1997, *Astroparticle Physics*, **7**, 183
 Berezhko E. G., Völk H. J., 2000, *A&A*, **357**, 283
 Berezhinskii V. S., Bulanov S. V., Dogiel V. A., Ptuskin V. S., 1990, *Astrophysics of cosmic rays*
 Blandford R. D., Ostriker J. P., 1980, *ApJ*, **237**, 793
 Braiding C., et al., 2018, *Publ. Astron. Soc. Australia*, **35**, e029
 Brand J., Blitz L., 1993, *A&A*, **275**, 67
 Brisken W. F., Carrillo-Barragán M., Kurtz S., Finley J. P., 2006, *ApJ*, **652**, 554
 Brose R., Pohl M., Sushch I., Petruk O., Kuzyo T., 2020, *A&A*, **634**, A59
 Burton M. G., et al., 2013, *Publ. Astron. Soc. Australia*, **30**, e044
 CTA Consortium Acharya B. S., Agudo I., Al Samarai I., Alfaro R., Alfaro J., 2018, *Science with the Cherenkov Telescope Array*, doi:10.1142/10986.
 Casanova S., et al., 2010, *PASJ*, **62**, 1127
 Celli S., Morlino G., Gabici S., Aharonian F. A., 2019, *MNRAS*, **490**, 4317
 Crutcher R. M., Wandelt B., Heiles C., Falgarone E., Troland T. H., 2010, *ApJ*, **725**, 466
 Devin J., Acero F., Ballet J., Schmid J., 2018, *A&A*, **617**, A5
 Dickey J. M., et al., 2013, *Publ. Astron. Soc. Australia*, **30**, e003
 Feijen K., Rowell G., Einecke S., Braiding C., Burton M. G., Maxted N., Voisin F., Wong G. F., 2020, *Publ. Astron. Soc. Australia*, **37**, e056
 Finley J. P., Oegelman H., 1994, *ApJ*, **434**, L25
 Fukui Y., et al., 2003, *PASJ*, **55**, L61
 Fukui Y., Sano H., Yamane Y., Hayakawa T., Inoue T., Tachihara K., Rowell G., Einecke S., 2021, *ApJ*, **915**, 84
 Gabici S., Aharonian F. A., Blasi P., 2007, *Ap&SS*, **309**, 365
 Gabici S., Aharonian F. A., Casanova S., 2009, *MNRAS*, **396**, 1629
 Giuliani A., et al., 2010, *A&A*, **516**, L11
 H. E. S. S. Collaboration et al., 2018a, *A&A*, **612**, A1
 H. E. S. S. Collaboration et al., 2018b, *A&A*, **612**, A2
 Heger A., Fryer C. L., Woosley S. E., Langer N., Hartmann D. H., 2003, *ApJ*, **591**, 288
 Hewitt J. W., Yusef-Zadeh F., 2009, *ApJ*, **694**, L16
 Kafexhiu E., Aharonian F., Taylor A. M., Vila G. S., 2014, *Phys. Rev. D*, **90**, 123014
 Kelner S. R., Aharonian F. A., Bugayov V. V., 2006, *Phys. Rev. D*, **74**, 034018
 Li H., Chen Y., 2010, *MNRAS*, **409**, L35
 Liu B., Yang R.-z., Sun X.-n., Aharonian F., Chen Y., 2019, *ApJ*, **881**, 94
 Lucek S. G., Bell A. R., 2000, *MNRAS*, **314**, 65
 Malkov M. A., Drury L. O., 2001, *Reports on Progress in Physics*, **64**, 429
 McClure-Griffiths N. M., Dickey J. M., Gaensler B. M., Green A. J., Haverkorn M., Strasser S., 2005, *ApJS*, **158**, 178
 Mitchell A. M. W., Rowell G. P., Celli S., Einecke S., 2021, *MNRAS*, **503**, 3522
 Nomoto K., Maeda K., Mazzali P. A., Umeda H., Deng J., Iwamoto K., 2004, *Hypernovae and Other Black-Hole-Forming Supernovae*. Springer Netherlands, doi:10.1007/978-0-306-48599-2_10, https://doi.org/10.1007/978-0-306-48599-2_10
 Ptuskin V. S., Zirakashvili V. N., 2005, *A&A*, **429**, 755
 Ptuskin V., Zirakashvili V., Seo E.-S., 2010, *ApJ*, **718**, 31
 Reynolds S. P., 2008, *ARA&A*, **46**, 89
 Sano H., et al., 2020, *ApJ*, **904**, L24
 Strong A. W., Moskalenko I. V., Ptuskin V. S., 2007, *Annual Review of Nuclear and Particle Science*, **57**, 285

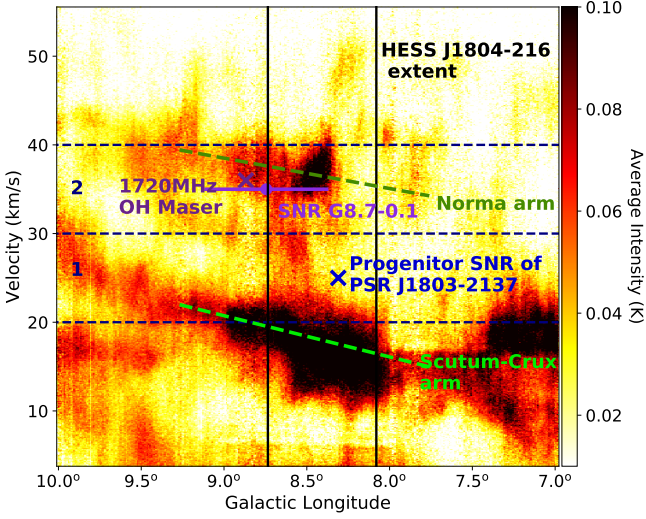


Figure A1. Position-velocity plot of Mopra $^{12}\text{CO}(1-0)$ emission (K) towards HESS J1804–216, integrated over latitudes from -0.49° to 0.49° . The black vertical lines show the longitudinal extent of HESS J1804–216. The blue cross indicates the birth position of PSR J1803–2137 at its assumed velocity of $\sim 25 \text{ km s}^{-1}$. The 1720MHz OH maser is shown by the purple cross at its velocity of 36 km s^{-1} . The centre of SNR G8.7–0.1 is shown by the purple dot, whilst the purple line shows its radial extent, at a velocity of 35 km s^{-1} . The green dashed lines are estimates of the Galactic spiral arms along the line of sight for HESS J1804–216 (from the model in Vallée 2014). Components 1 and 2 are indicated by the dashed navy lines.

Vallée J. P., 2014, *AJ*, 148, 5

Zirakashvili V. N., Aharonian F. A., 2010, *ApJ*, 708, 965

APPENDIX A: POSITION-VELOCITY PLOTS

Figs. A1 and A2 are position-velocity plots for the $^{12}\text{CO}(1-0)$ and HI data, respectively, towards the HESS J1804–216 region, integrated over latitudes $b = -0.49^\circ$ to 0.49° . Using this figure we defined two gas velocity regions, Component 1 ($v_{\text{lsr}} = 20$ to 30 km s^{-1}) and Component 2 ($v_{\text{lsr}} = 30$ to 40 km s^{-1}), as shown by the dashed navy lines.

APPENDIX B: ADDITIONAL MODEL TERMS

The onset of the Sedov-Taylor phase is defined in Celli et al. (2019):

$$t_{\text{sedov}} \sim 1.6 \times 10^3 \left(\frac{E_{\text{SN}}}{10^{51} \text{ erg}} \right)^{-1/2} \left(\frac{M_{\text{ej}}}{10 M_{\odot}} \right)^{5/6} \text{ yr} \quad (\text{B1})$$

where E_{SN} is the ejected supernova total kinetic energy and M_{ej} is the mass of the ejecta.

The inelastic cross-section of proton-proton collisions is taken from the most recent parameterisation by Kafexhiu et al. (2014).

$$\sigma_{\text{pp}}(E_p) = \left[30.7 - 0.96 \ln \left(\frac{E_p}{E_p^{\text{th}}} \right) + 0.18 \ln \left(\frac{E_p}{E_p^{\text{th}}} \right)^2 \right] \times \left[1 - \left(\frac{E_p^{\text{th}}}{E_p} \right)^{1.9} \right]^3 \text{ mbarn} \quad (\text{B2})$$

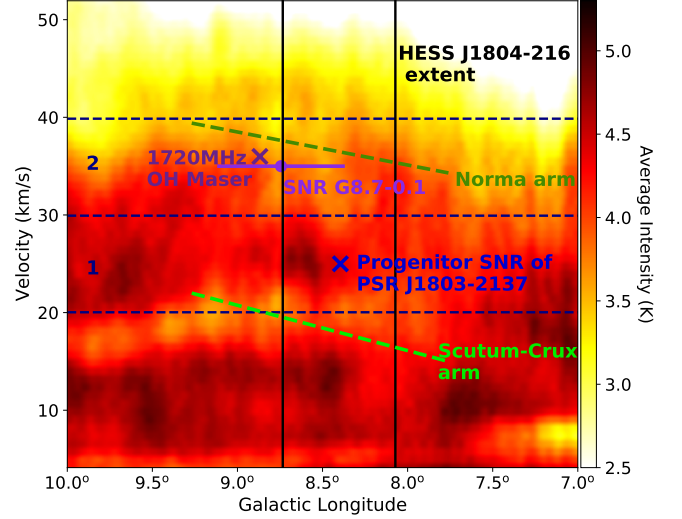


Figure A2. Position-velocity plot of SGPS HI emission (K) towards HESS J1804–216. The annotations are described in Fig. A1.

where E_p is the kinetic energy of the proton and $E_p^{\text{th}} = 2m_{\pi} + m_{\pi}^2/2m_p \sim 0.2797 \text{ GeV}$ is the threshold kinetic energy.

The total γ -ray spectrum is given by equation (B3), for simplicity $x = E_{\gamma}/E_p$.

$$F_{\gamma}(x, E_p) = B_{\gamma} \frac{\ln(x)}{x} \left(\frac{1 - x^{\beta_{\gamma}}}{1 + k_{\gamma} x^{\beta_{\gamma}} (1 - x^{\beta_{\gamma}})} \right)^4 \times \left[\frac{1}{\ln(x)} - \frac{4\beta_{\gamma} x^{\beta_{\gamma}}}{1 - x^{\beta_{\gamma}}} - \frac{4k_{\gamma} \beta_{\gamma} x^{\beta_{\gamma}} (1 - 2x^{\beta_{\gamma}})}{1 + k_{\gamma} x^{\beta_{\gamma}} (1 - x^{\beta_{\gamma}})} \right] \quad (\text{B3})$$

The additional parameters, B_{γ} , β_{γ} and k_{γ} , are an approximation from numerical calculation using the best least square fit and dependent on the energy of the CR protons. For the proton energy range from $0.1 - 10^5 \text{ TeV}$ these parameters are defined as:

$$\begin{aligned} B_{\gamma} &= 1.3 + 0.14L + 0.011L^2 \\ \beta_{\gamma} &= (1.79 + 0.11L + 0.008L^2)^{-1} \\ k_{\gamma} &= (0.801 + 0.049L + 0.014L^2)^{-1} \end{aligned} \quad (\text{B4})$$

APPENDIX C: HESS J1804–216 SPECTRAL COMPARISON

Fig. C1 shows the spectral comparison between the H.E.S.S. 2006 survey of the inner galaxy (Aharonian et al. 2006) and the 2018 HGPS data (H. E. S. S. Collaboration et al. 2018a) towards HESS J1804–216. These spectra tend to match well. The observations from Aharonian et al. (2006) are between May and July of 2004 with 11.7 hr of observation time. The data from H. E. S. S. Collaboration et al. (2018a) was collected between January of 2006 and January of 2013 with ~ 44 hr of observations. Aharonian et al. (2006) provide a dedicated source analysis on HESS J1804–216 with more spectral data points than H. E. S. S. Collaboration et al. (2018a) which has a total of six bins (fixed bin number for all sources). The data from Aharonian et al. (2006) is utilised here, as we want to compare the spectral shape of the observations with our model.

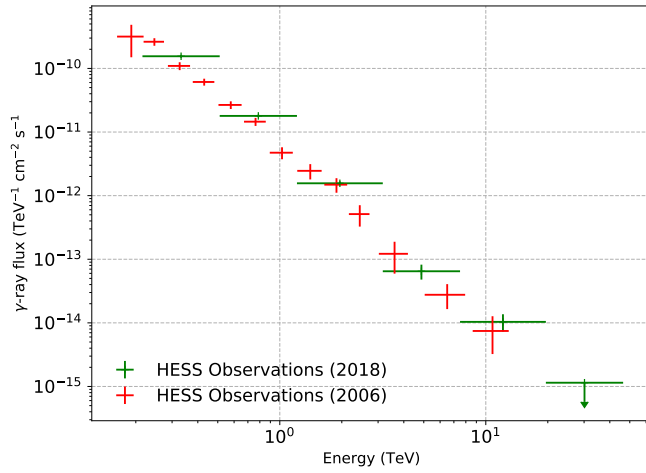


Figure C1. TeV γ -ray spectra towards HESS J1804–216 from [Aharonian et al. \(2006\)](#) in red and [H. E. S. S. Collaboration et al. \(2018a\)](#) in green. [Aharonian et al. \(2006\)](#) has more spectral points as this involved a dedicated source analysis on HESS J1804–216.

APPENDIX D: BEST MATCHING MODELS

The following tables show the model parameters for the best matching spectral models based on their χ^2/m values, shown here in ascending order. Each model is given a name identifier, used within the main text.

This paper has been typeset from a \TeX/L\AA\TeX file prepared by the author.

Table D1. The 5 best matching spectral models for accelerator SNR G8.7–0.1 for an age of 15 kyr with their model parameters.

Model name	α	χ	δ	δ_p	$E_{p,max}$ (PeV)	SN Type	M_{ej} (M_\odot)	E_{SN} (erg)	W_p (10^{49} erg)	$E_{p,esc}$ (TeV)	χ^2/m (Spectral)	S (Spatial, 10^{-13})
G1a	2.0	0.001	0.5	1.4	5.0	Ia	1	10^{51}	7.0	14.8	1.0	2.8
G2a	2.0	0.001	0.4	2.5	5.0	II	10	10^{51}	6.9	18.6	1.1	3.2
G3a	2.0	0.01	0.3	1.4	5.0	Ia	1	10^{51}	7.0	14.8	1.1	3.0
G4a*	2.0	0.01	0.6	2.5	1.0	II	20	10^{51}	6.2	15.7	1.1	2.7
G5a	2.0	0.001	0.4	2.5	1.0	II	20	10^{51}	6.2	15.7	1.1	2.8

* Best spatial model

Table D2. The 5 best matching spectral models for accelerator SNR G8.7–0.1 for an age of 28 kyr with their model parameters.

Model name	α	χ	δ	δ_p	$E_{p,max}$ (PeV)	SN Type	M_{ej} (M_\odot)	E_{SN} (erg)	W_p (10^{50} erg)	$E_{p,esc}$ (TeV)	χ^2/m (Spectral)	S (Spatial, 10^{-13})
G1b	1.8	0.01	0.6	1.4	5.0	Ia	1	10^{51}	1.5	6.2	0.6	1.9
G2b*	1.8	0.1	0.4	1.4	5.0	Ia	1	10^{51}	1.5	6.2	0.8	1.6
G3b	1.8	0.001	0.4	1.4	1.0	II	20	10^{52}	1.0	8.1	1.0	2.3
G4b	2.0	0.001	0.4	1.4	5.0	II	10	10^{52}	0.7	18.1	1.0	3.2
G5b	1.8	0.1	0.4	1.4	1.0	II	20	10^{52}	1.0	8.1	1.0	2.0

* Best spatial model

Table D3. The 5 best matching spectral models for accelerator progenitor SNR of PSR J1803–2137 for an age of 16 kyr with their model parameters.

Model name	α	χ	δ	δ_p	n_0 (cm^{-3})	$E_{p,max}$ (PeV)	SN Type	M_{ej} (M_\odot)	E_{SN} (erg)	W_p (10^{49} erg)	$E_{p,esc}$ (TeV)	χ^2/m (Spectral)	S (Spatial, 10^{-13})
P1*	1.8	0.01	0.6	2.5	20	5.0	II	20	10^{52}	3.8	3.8	0.9	1.2
P2	1.8	0.01	0.6	2.5	10	5.0	II	20	10^{52}	4.5	3.8	0.9	1.4
P3	1.8	0.001	0.3	1.4	20	1.0	II	10	10^{52}	2.6	8.0	1.0	2.6
P4	1.8	0.01	0.6	2.5	1	5.0	II	20	10^{52}	8.7	3.8	1.0	2.6
P5	2.0	0.001	0.4	2.5	0.1	1.0	II	20	10^{51}	3.5	13.4	1.0	1.2

* Best spatial model